Preparation and Mechanical Properties of Zr-based Bulk Nanocrystalline Alloys Containing Compound and Amorphous Phases

Cang Fan[†], Akira Takeuchi and Akihisa Inoue

Institute for Materials Research, Tohoku University, Sendai 980-8577, Japan

Bulk nanocrystalline alloys with good ductility and high tensile strength (σ_f) in Zr–Al–Cu–Pd and Zr–Al–Cu–Pd–Fe systems were formed by partial crystallization of cast bulk amorphous alloys. The nanostructure alloys consist of nanoscale $Zr_2(Cu, Pd)$ compound surrounded by the remaining amorphous phase. The particle size and interparticle spacing of the compound are less than 10 and 2 nm, respectively. The crystallization of a ternary $Zr_{60}Al_{10}Cu_{30}$ amorphous alloy occurs by the simultaneous precipitation of Zr_2Al and Zr_2Cu phases with large particle size of about 500 nm and hence the addition of Pd is essential for formation of the nanostructure. The nanostructure alloys in the cast cylinder of 2 to 3 mm in diameter keep good ductility in the volume fraction (V_f) range of the compound phase below 20 to 40%. The σ_f, Young's modulus (E) and fracture elongation (ε) increase from 1760 MPa, 81.5 GPa and 2.10%, respectively, at $V_f=0\%$ to 1880 MPa, 89.5 GPa and 2.17%, respectively, at $V_f=40\%$ for the $Zr_{60}Al_{10}Cu_{20}Pd_{10}$ alloy and from 1750 MPa, 81.1 GPa and 2.21%, respectively, at $V_f=0\%$ to 1850 MPa, 85.6 GPa and 2.28%, respectively, at $V_f=28\%$ for the $Zr_{60}Al_{10}Cu_{15}Pd_{10}Fe_5$ alloy. The formation of the bulk nanostructure alloys with high σ_f and good ductility in coexistent with the compound is presumably because the remaining amorphous phase can contain a number of free volumes by water quenching from the supercooled liquid region. The synthesis of the high-strength bulk amorphous alloys containing nanoscale compounds is important for future development of a new type of high-strength material.

(Received April 21, 1998; In Final Form September 24, 1998)

Keywords: *bulk nanocrystalline alloy, partial crystallization, copper mold casting, zirconium base alloy, nanoscale compound, compositional effect, high mechanical strength*

I. Introduction

Nanocrystalline alloys with useful characteristics have been synthesized by partial crystallization of an amorphous phase in a number of melt-spun alloys such as Fe–Nd–B[1]-[3], Fe–Si–B–Nb–Cu[4], Fe–(Zr, Nb)–B[5], Al–Ln–TM[6][7] (Ln=lanthanide metal, TM=transition metal) and Mg–Ln–TM[8] etc. The nanocrystallization process has a great advantage of forming a nanocrystalline alloy in a ribbon form. The material form has enabled the application of their nanocrystalline alloys as engineering materials[9]. As engineering characteristics which have not been obtained for conventional crystalline alloys, one can list up hard magnetism[1]-[3], soft magnetism[4][5], high tensile strength[6]-[8] and high sensitive magnetostriction[10]. However, the shape and dimension of the nanocrystalline alloys have been limited to the ribbon form with a thickness less than about 30 μm and the powder form with a diameter of less than about 40 μm. Thus, no bulk nanocrystalline alloys containing a residual amorphous phase have been synthesized by any kinds of preparation techniques reported hitherto. The synthesis of a bulk nanocrystalline alloy with similar useful characteristics to the ribbon-form amorphous alloy is expected to cause a further extension of application fields of

nanocrystalline alloys.

Recently, a number of bulk amorphous alloys have been formed by copper mold casting processes in Mg–Ln–TM[11], Ln–Al–TM[12], Zr–Al–TM[13], Zr–(Ti, Nb, Pd)–Al–TM[14], Zr–Ti–TM–Be[15], Fe–(Al, Ga)–(P, C, B, Si)[16], Pd–Cu–Ni–P[17], Pd–Ni–Fe–P[18], (Fe, Co, Ni)–(Zr, Nb, Ta)–B[19], Fe–Co–(Zr, Nb)–(Mo, W)–B[20] and Co–Fe–(Zr, Nb, Ta)–B[21] systems. Consequently, if a bulk amorphous alloy with nanostructure in crystallization process is found, we can develop a simple preparation process of a bulk nanocrystalline alloy by a method of the formation of a bulk amorphous alloy, followed by partial crystallization. More recently, it has been found[22] that the addition of Pd, Au or Pt element into melt-spun Zr–Al–Cu amorphous alloys induces the formation of a nanostructure consisting of $Zr_2(Cu, M)$ (M=Pd, Au or Pt) and remaining amorphous phases, and the nanostructure alloys can keep better bending ductility and higher tensile fracture strength as compared with those for the corresponding amorphous single phase alloys. These novel results allow us to expect that bulk nanocrystalline alloys with high tensile fracture strength and good ductility are synthesized in the Zr–Al–Cu alloys containing an appropriate amount of Pd, Au or Pt element. This paper is intended to present the changes in the structure and mechanical properties by nanocrystallization for the Zr–Al–Cu–M (M=Pd or Au) amorphous alloys in melt-spun ribbon and cast bulk forms and to investigate the mechanisms for the formation of the nanostructure and for the achievement of high tensile strength and good ductility even for the bulk alloys.

II. Experimental Procedure

Multicomponent alloys with compositions of $Zr_{60}Al_{10}Cu_{30-x}Pd_x$, $Zr_{60}Al_{10}Cu_{30-x}Au_x$ ($x=0$, 5, 8 and 10 at%) and $Zr_{60}Al_{10}Cu_{15}Pd_{10}Fe_5$ were examined in the present study because the $Zr_{60}Al_{10}Cu_{30}$ amorphous alloy has a wide supercooled liquid region before crystallization and a high glass-forming ability leading to the formation of a bulk amorphous alloy with diameters up to about 10 mm. The alloy ingots were prepared by arc melting of pure Zr, Al, Cu, Pd, Au and Fe metals in an argon atmosphere. Using the ingots, rapidly solidified ribbons with a thickness of about 30 μm were prepared by melt spinning in an argon atmosphere. Bulk cylindrical alloys with diameters of 4 to 6 mm were prepared by the copper mold casting method. Subsequent annealing treatment was made for different times in the temperature range between T_g and T_x.

The structure in as-prepared and annealed states of the alloys was examined by X-ray diffractometry and transmission electron microscopy (TEM). The distribution of alloy components was examined by high-resolution TEM and nanobeam energy dispersive X-ray (EDX) spectroscopy. Thermal stability of the alloys was examined by differential scanning calorimetry (DSC) at a heating rate of 0.67 K/s. The heat of crystallization (ΔH) of the Zr-based amorphous alloys is roughly independent of composition, and hence the crystalline fraction (V_f) of the specimens was determined from the ratio of the amount of heat released on being heated from room temperature to 850 K to the amount of heat evolved from a totally amorphous specimen on crystallization, using the following equation.

$$V_f = (\Delta H_{T,Am} - \Delta H_{T,PAm}) / \Delta H_{T,Am}.$$

Here, $\Delta H_{T,Am}$ is the total enthalpy released upon crystallization of a totally amorphous sample and $\Delta H_{T,PAm}$ is the total enthalpy released upon crystallization of a partially amorphous sample. Tensile strength, Young's modulus and elongation were measured with an Instron testing machine combined with a strain gauge meter. The tensile test was carried out at room temperature and at a strain rate of $8.3 \times 10^{-3}\,s^{-1}$ for the bulk cylindrical and ribbon samples. Vickers hardness was measured with a Vickers microhardness tester under a load of 2.55 N (25 gf). Fracture appearance after the tensile test was examined by scanning electron microscopy (SEM).

III. Results

1. Nanocrystallized structure and mechanical properties of the melt-spun alloys

Figure 1 shows the DSC curves of the melt-spun amorphous $Zr_{60}Al_{10}Cu_{30-x}Pd_x$ ($x=0$ and 10 at%) alloys. Although the Zr–Al–Cu amorphous alloy crystallizes by a single exothermic reaction in the supercooled liquid region, the Pd-containing alloys show two exothermic
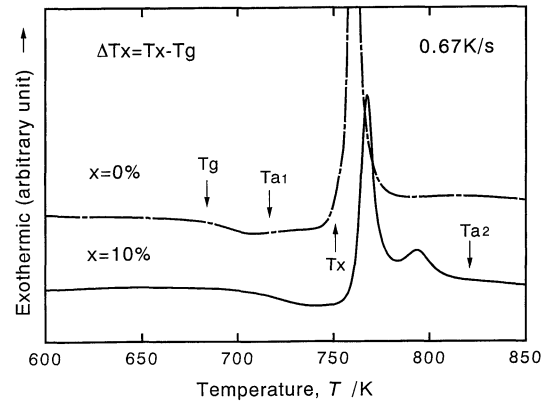

Fig. 1 Change in the DSC curves of melt-spun amorphous $Zr_{60}Al_{10}$-$Cu_{30-x}Pd_x$ ($x=0$ and 10 at%) alloys with Pd content.
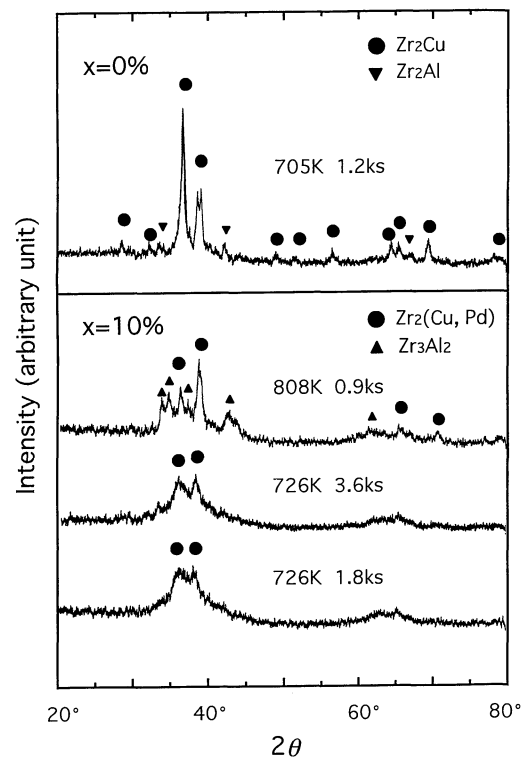

Fig. 2 X-ray diffraction patterns of melt-spun amorphous $Zr_{60}Al_{10}$-$Cu_{30-x}Pd_x$ ($x=0$ and 10 at%) alloys annealed in different conditions.

peaks. It is seen that the extra exothermic peak appears at the higher temperature side. **Figure 2** shows the X-ray diffraction patterns of the $Zr_{60}Al_{10}Cu_{30-x}Pd_x$ ($x=0$ and 10 at%) alloys annealed for 1.2 to 3.6 ks at 705 and 726 K in the supercooled liquid region. The diffraction pattern of the Pd-containing alloy shows the existence of amorphous and bct-Zr_2Cu phases, and the intensity and the half width of the Zr_2Cu diffraction peaks change significantly by the addition of Pd. That is, the Pd-containing alloys have much lower intensity and broader peak, suggesting that the Zr_2Cu phase has a much smaller grain size in $Zr_{60}Al_{10}Cu_{20}Pd_{10}$ than in $Zr_{60}Al_{10}Cu_{30}$ alloy. In order to confirm the formation of the nanoscale mixed

structure, the TEM image and selected-area electron diffraction pattern of the $Zr_{60}Al_{10}Cu_{20}Pd_{10}$ alloy annealed at 726 K for different periods are shown in **Fig. 3**. The annealed alloy consists mainly of very fine Zr_2Cu grains with sizes of less than 10 nm at 1.8 ks, 20 nm at 2.4 ks and 25 nm at 3.6 ks. The diffraction patterns contain distinct halo rings in addition to the spotty reflection rings resulting from Zr_2Cu phase. The V_f of the Zr_2Cu phase is estimated to be 75% at 1.8 ks, 82% at 2.4 ks and 95% at 3.6 ks from the change in the heat of exothermic reaction on the DSC curve due to the precipitation of the Zr_2Cu phase.

The distribution of the solute elements in the nanostructure was examined by high resolution TEM and nanobeam EDX analyses. **Figure 4** shows the high-resolution TEM image and EDX profiles taken from both the Zr_2Cu compound and amorphous phase regions in the $Zr_{60}Al_{10}Cu_{20}Pd_{10}$ alloy. It is recognized that Pd is dissolved into the Zr_2Cu phase while Al is segregated into the remaining amorphous phase. Consequently, the chemical formula of the compound is expressed as $Zr_2(Cu, Pd)$. The enrichment of Al into the remaining amorphous phase may cause the increase in the thermal stability of the remaining amorphous phase, resulting in the formation of the mixed structure.

Here, it is important to point out that the mixed phase alloys in the ribbon form exhibit good bending ductility and can be bent through 180 degrees without fracture. By using the ductile ribbon samples, the mechanical properties were examined as a function of V_f of Zr_2Cu phase. **Figure 5** shows the changes in the tensile fracture strength (σ_f), Vickers hardness (H_v) and Young's modulus (E) with volume fraction (V_f) of the Zr_2Cu phase for the melt-spun $Zr_{60}Al_{10}Cu_{20}Pd_{10}$ amorphous ribbon. The σ_f, H_v and E increase almost linearly with increasing V_f in the wide V_f range up to about 75% and the increasing ratio is about 18% for σ_f, 20% for H_v and 19% for E.

However, with further increasing V_f, the ribbon sample becomes brittle, leading to a rapid decrease in σ_f. In order to confirm the maintenance of the good ductility for the amorphous alloy, scanning electron micrographs of the tensile fracture surface of the as-spun ribbon and the annealed ribbon with $V_f=75\%$ exhibiting the highest σ_f are shown in **Fig. 6**. From the comparison of their fracture surfaces, it is clearly recognized that the smooth region marked with an arrow in the fracture surafce increases significantly for the mixed phase alloy. The increase in the smooth region implies the increase in the amount of shear deformation before final adiabatic fracture, indicating that the mixed phase alloy has good ductility which enables the significant shear deformation.

The two-stage crystallization process and the formation of the nanostructure alloys have also been recognized for the $Zr_{60}Al_{10}Cu_{30-x}Au_x$ ($x=5$ to 8 at%) alloys. **Table 1** summarizes the T_g, T_{x1}, T_{x2} and $\Delta T_x(=T_{x1}-T_g)$ of the $Zr_{60}Al_{10}Cu_{30}$, $Zr_{60}Al_{10}Cu_{20}Pd_{10}$, $Zr_{60}Al_{10}Cu_{22}Au_8$ and $Zr_{60}Al_{10}Cu_{15}Pd_{10}Fe_5$ amorphous alloys. Here, T_{x1} and T_{x2} represent the onset temperatures of the first and second exothermic peaks due to crystallization, respectively. **Figure 7** shows the TEM image and selected-area electron diffraction pattern of the 8%Au-containing alloy annealed for 1.2 ks at 738 K between T_g and T_{x1}. The structure also consists of fine Zr_2Cu grains with a size of about 10 nm. Distinct halo rings are also seen in the diffraction patterns, revealing the existence of the remaining amorphous phase. The structural feature is the same as that for the Pd-containing alloys shown in Fig. 2. **Figure 8** also shows the changes in the σ_f, H_v and E with V_f for the 8 %Au-containing alloy. These strength values also show a linear increase in the wide V_f range up to 75% and the highest values of σ_f and H_v are 2030 MPa and 620, respectively, being nearly the same as those for the Pd-containing alloy.
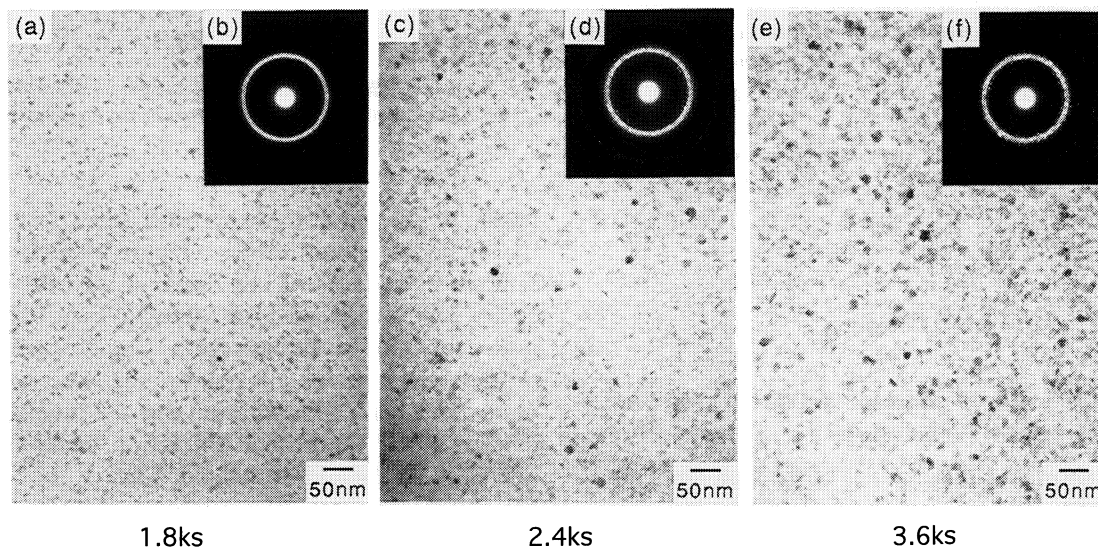

Fig. 3   Bright-field electron micrographs and selected-area electron diffraction patterns of melt-spun amorphous $Zr_{60}Al_{10}$-$Cu_{20}Pd_{10}$ alloy annealed at 726 K for 1.8, 2.4 and 3.6 ks.
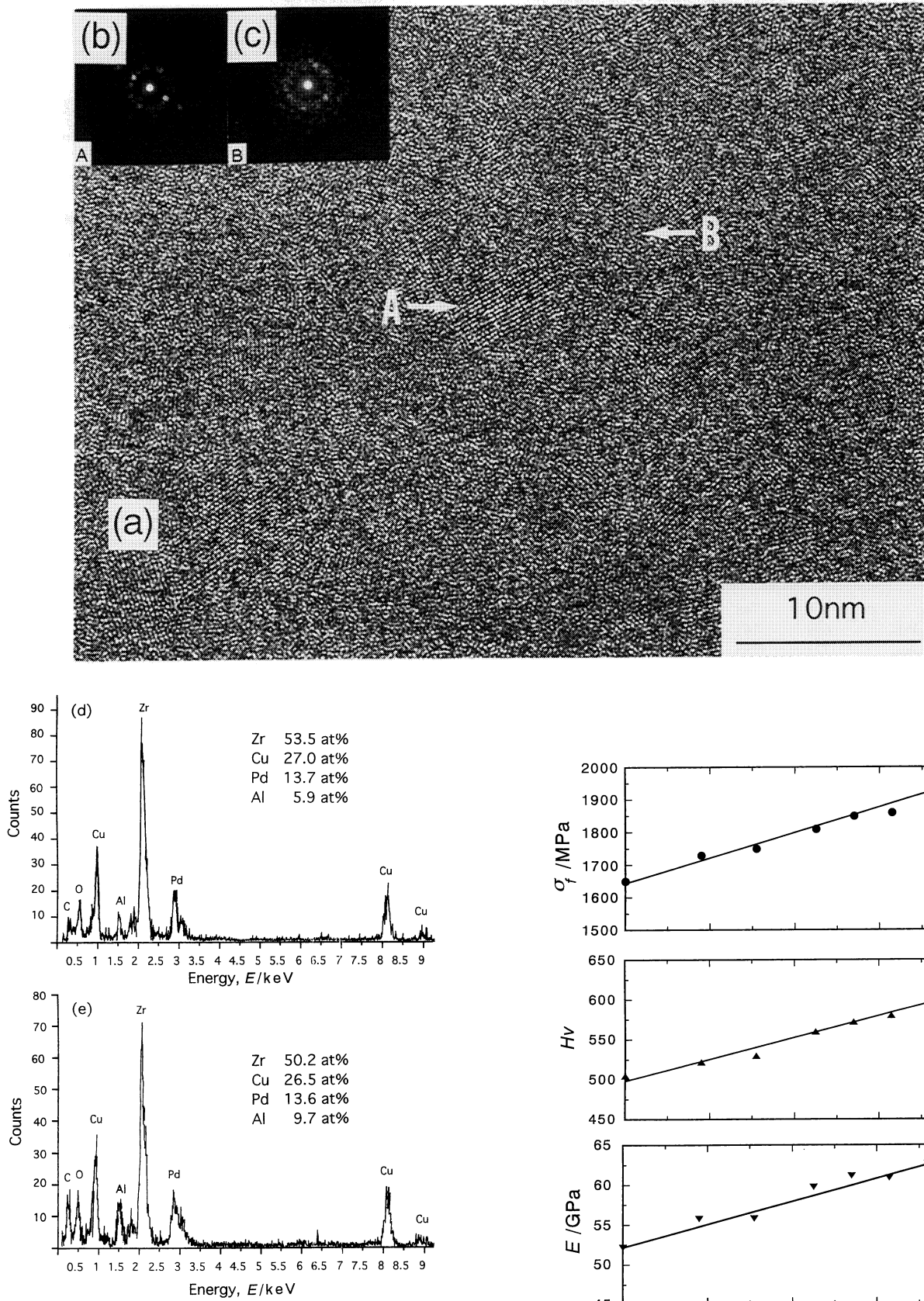
Fig. 4 High-resolution TEM image and nanobeam EDX spectroscopy profiles taken from the amorphous and compound phases in melt-spun amorphous $Zr_{60}Al_{10}Cu_{20}Pd_{10}$ alloy annealed at 726 K for 1.2 ks. The diffraction patterns (b) and (c) were taken from regions A and B, respectively, in (a). The EDX profiles (d) and (e) were also taken from regions A and B, respectively.
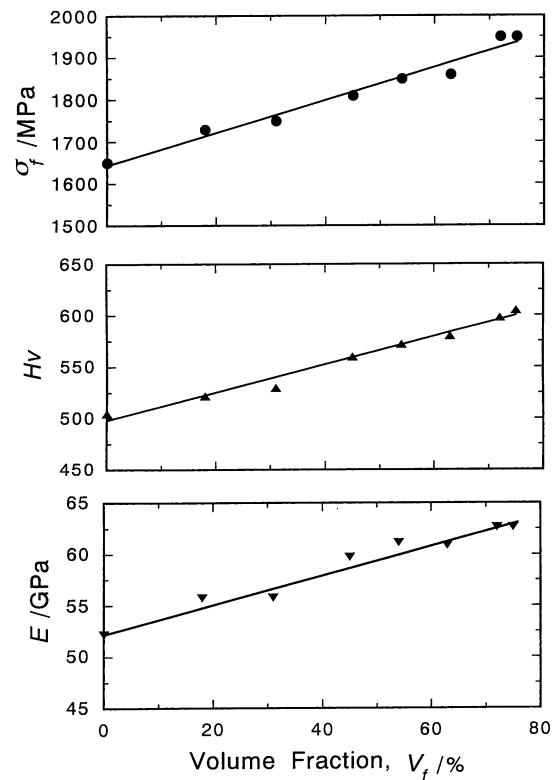
Fig. 5 Changes in the tensile fracture strength (σ_f), Vickers hardness (H_v) and Young's modulus (E) with V_f of Zr_2Cu phase for melt-spun amorphous $Zr_{60}Al_{10}Cu_{20}Pd_{10}$ alloy.
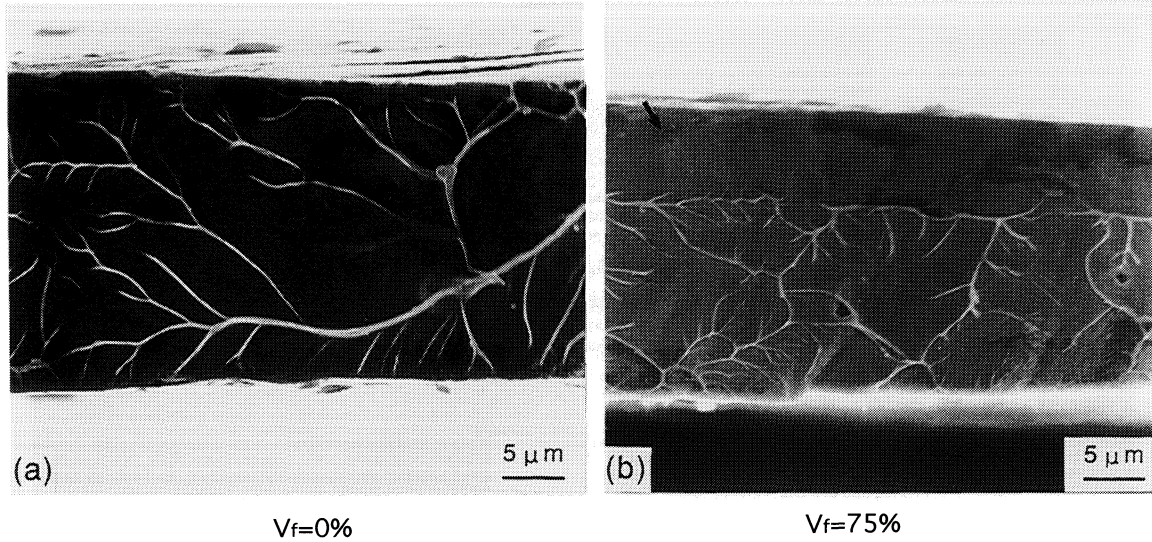
Fig. 6   Tensile fracture surface appearance of melt-spun amorphous $Zr_{60}Al_{10}Cu_{20}Pd_{10}$ alloy with V_f of 0% (a) and 75% (b). An arrow in (b) represents a smooth region caused by shear sliding.

Table 1   Thermal stability of Zr–Al–Cu, Zr–Al–Cu–M (M=Pd or Au) and Zr–Al–Cu–Pd–Fe amorphous alloys.

Alloys (at%)	T_g/K	T_{x1}/K	T_{x2}/K	$\Delta T_x\ (=T_{x1}-T_g)$
$Zr_{60}Al_{10}Cu_{30}$	676	748	—	72
$Zr_{60}Al_{10}Cu_{20}Pd_{10}$	699	761	784	62
$Zr_{60}Al_{10}Cu_{22}Au_8$	721	783	808	62
$Zr_{60}Al_{10}Cu_{15}Pd_{10}Fe_5$	699	769	797	70

T_g: glass transition temperature.
T_{x1}: onset temperature of the first exothermic peak.
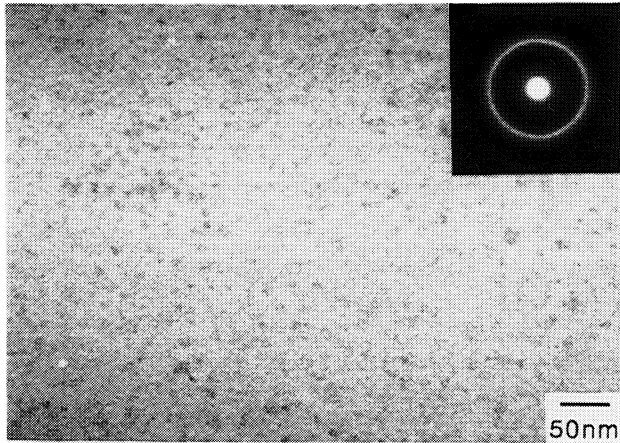T_{x2}: onset temperature of the second exothermic peak.

Fig. 7   Bright-field electron micrographs and selected-area electron diffraction patterns of melt-spun amorphous $Zr_{60}Al_{10}Cu_{22}Au_8$ alloy annealed for 1.2 ks at 738 K.

2. Kinetic analyses of nanocrystallization

In order to clarify the effect of additional Pd or Au element on the formation of the nanocrystalline structure from the supercooled liquid of the Zr–Al–Cu alloys with high glass-forming ability, we examined the change in the crystallization kinetics with the addition of Pd or Au ele-
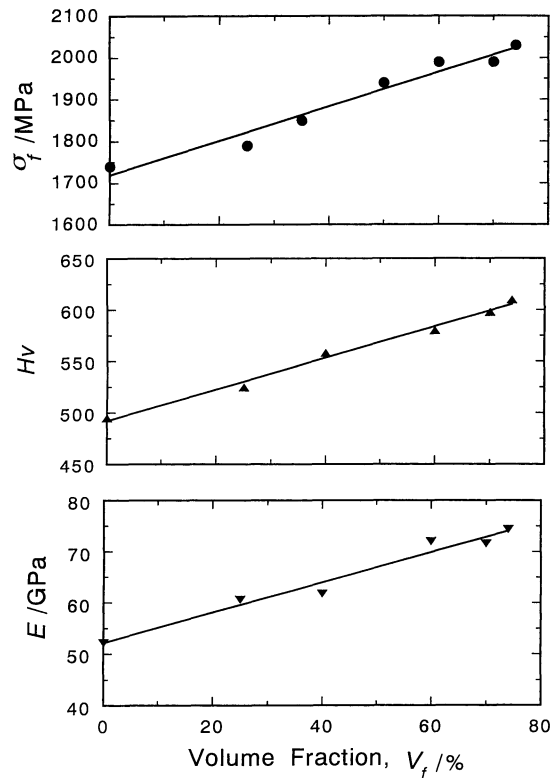

Fig. 8   Changes in the σ_f, H_v and E with V_f of Zr_2Cu phase for melt-spun $Zr_{60}Al_{10}Cu_{22}Au_8$ alloy.

ment. **Figure 9** shows the change in the first exothermic peak due to the precipitation of the $Zr_2(Cu, Pd)$ or $Zr_2(Cu, Au)$ phase during isothermal annealing at different temperatures for the $Zr_{60}Al_{10}Cu_{20}Pd_{10}$ and $Zr_{60}Al_{10}Cu_{22}Au_8$ amorphous alloys, together with the data of the $Zr_{65}Al_{7.5}Cu_{27.5}$ amorphous alloy. With increasing annealing temperature, the peak position shifts to a shorter time side and the peak intensity increases monotonously for all alloys. The transformation ratio
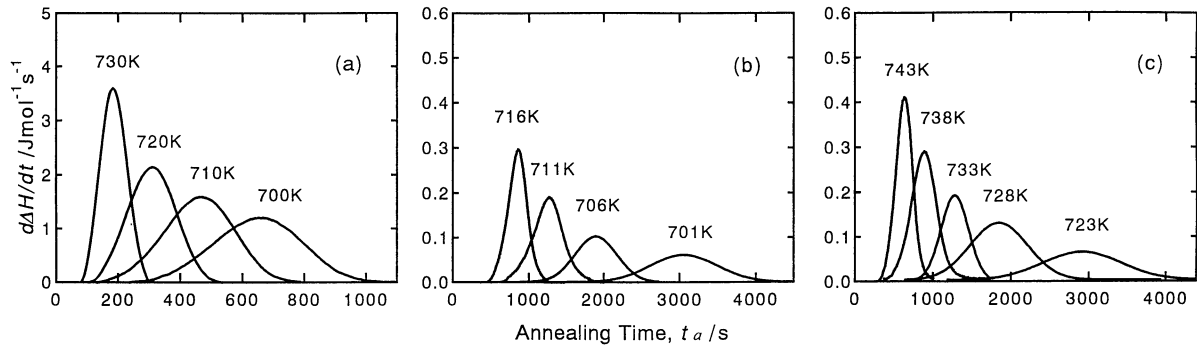
Fig. 9 Change in the DSC curves due to crystallization with isothermal annealing time at different temperatures for (a) $Zr_{65}Al_{7.5}Cu_{27.5}$, (b) $Zr_{60}Al_{10}Cu_{20}Pd_{10}$ and (c) $Zr_{60}Al_{10}Cu_{22}Au_8$ amorphous alloys.
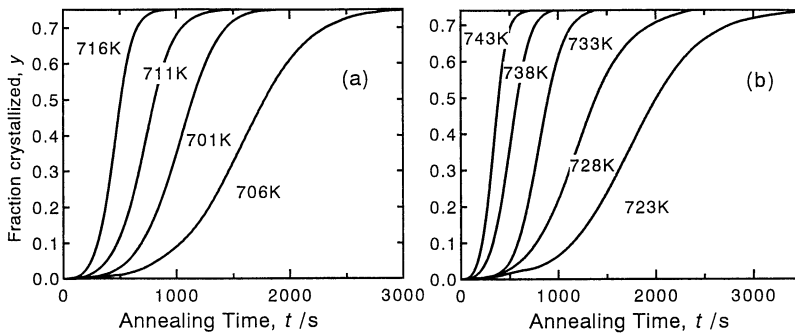
Fig. 10 Change in the transformation ratio (y) from amorphous to Zr_2Cu phase with isothermal annealing time (t_a) at various temperatures for (a) $Zr_{60}Al_{10}Cu_{20}Pd_{10}$ and (b) $Zr_{60}Al_{10}Cu_{22}Au_8$ amorphous alloys.
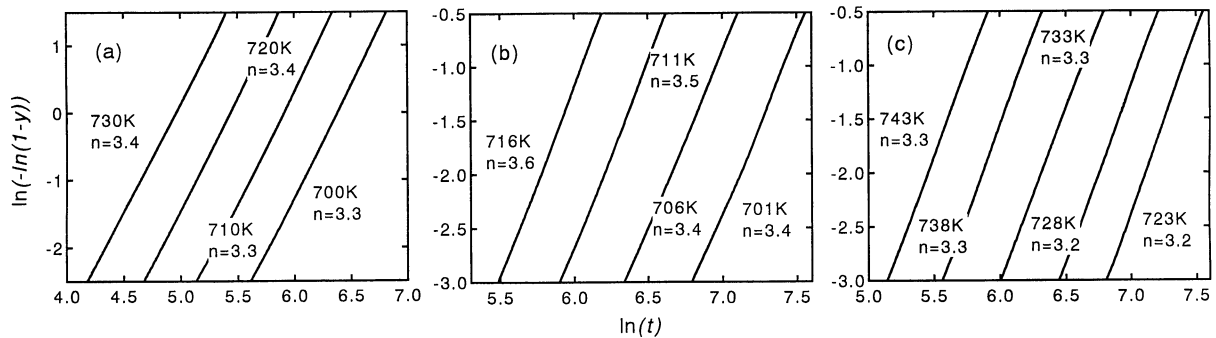
Fig. 11 Johnson-Mehl-Avrami plots between $\ln(-\ln(1-y))$ and $\ln(t)$ for crystallization for (a) $Zr_{65}Al_{7.5}Cu_{27.5}$, (b) $Zr_{60}Al_{10}Cu_{20}Pd_{10}$ and (c) $Zr_{60}Al_{10}Cu_{22}Au_8$ amorphous alloys.

(y) corresponding to the crystalline fraction (V_f), from amorphous to Zr_2Cu phase as a function of isothermal annealing time (t_a) excluding the incubation time increases along the sigmoidal curve as shown for the $Zr_{60}Al_{10}Cu_{20}Pd_{10}$ and $Zr_{60}Al_{10}Cu_{22}Au_8$ alloys in **Fig. 10**. The y values between 0.1 and 0.9 were used for the subsequent analysis in the framework of Johnson-Mehl-Avrami equation[23]. **Figure 11** shows the relation between $\ln(-\ln(1-y))$ and $\log(t)$ at various annealing temperatures. The good linear relation is recognized at all annealing temperatures and the slope of the linear relation corresponds to Avrami exponent (n value). The n value is evaluated to be 3.3 to 3.4 for the Zr-Al-Cu alloy, 3.4 to 3.6 for the Zr-Al-Cu-Pd alloy and 3.2 to 3.3 for the Zr-Al-Cu-Au alloy. From the n values, it is presumed that the crystallization of the Zr-Al-Cu amor-

phous alloy occurs by the polymorphic reaction in which the nucleation rate decreases continuously, while the Pd- and Au-containing alloys crystallize by the diffusion-controlled growth reaction in which all precipitates growing from small dimensions have an increasing nucleation rate[24][25]. We also measured the activation energy for the first-stage crystallization reaction corresponding to the precipitation of the nanocrystalline phase for the Pd- and Au-containing amorphous alloys. **Figure 12** summarizes the activation energies which were evaluated by the Arrhenius plot of the isothermal annealing data and the Kissinger plot of the continuous heating data, together with the data of the Zr-Al-Cu amorphous alloy. The activation energy is 1.9 to 2.2 eV for the Zr-Al-Cu alloy, 3.2 to 3.6 eV for the Zr-Al-Cu-Pd alloy and 3.2 to 3.8 eV for the Zr-Al-Cu-Au alloy. Thus, the activation energies
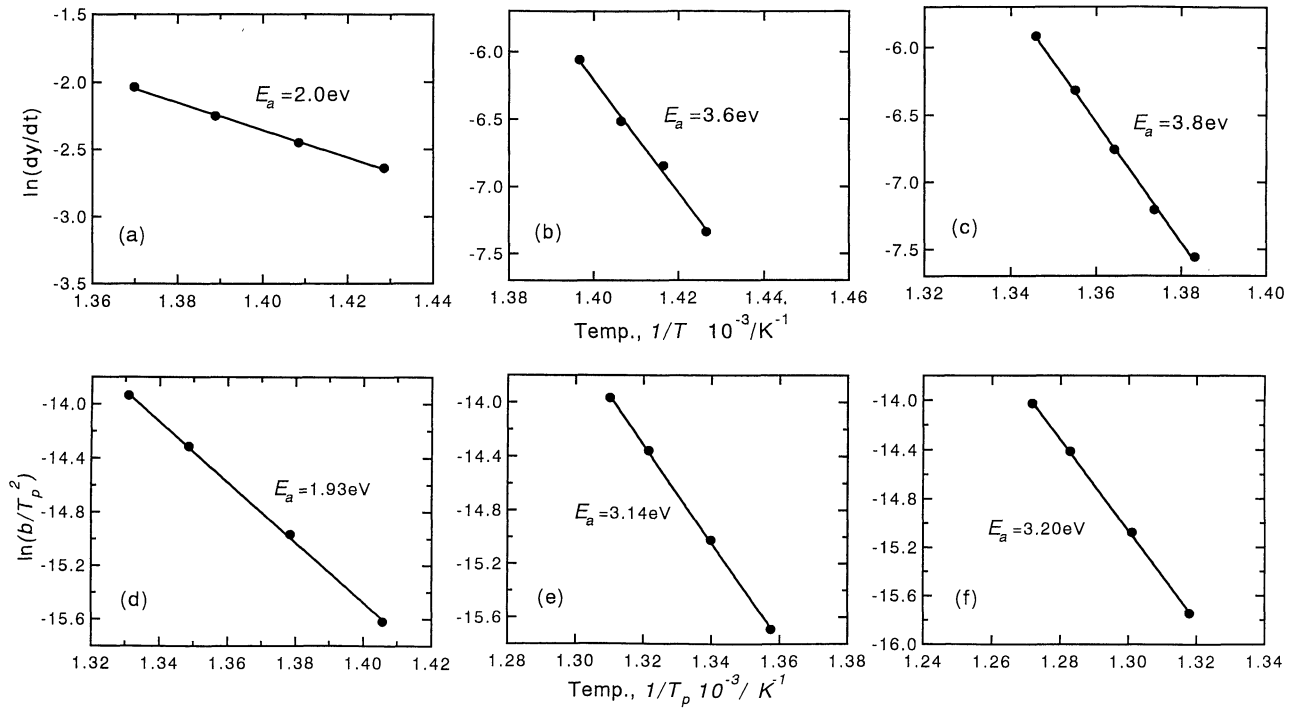
Fig. 12   Activation energies for the first-stage crystallization from Arrhenius plots to the Kissinger plots for (a, d) $Zr_{65}Al_{7.5}Cu_{27.5}$, (b, e) $Zr_{60}Al_{10}Cu_{20}Pd_{10}$ and (c, f) $Zr_{60}Al_{10}Cu_{22}Au_8$ amorphous alloys.

of the Pd- and Au-containing alloys are much larger than those for the Zr–Al–Cu alloy, indicating that the formation of the nanostructure is partly due to the difficulty of crystallization reaction caused by the necessity of the much higher activation energies. The mechanism for the formation of the nanostructure will be discussed later.

3.   Preparation and mechanical properties of bulk nanocrystalline alloys

Figure 13 shows the outer shape and surface appearance of the cast bulk amorphous $Zr_{60}Al_{10}Cu_{20}Pd_{10}$ and $Zr_{60}Al_{10}Cu_{15}Pd_{10}Fe_5$ cylinders with diameters of 4 and 6 mm, respectively. These cylindrical samples have smooth surface and metallic luster. Neither ruggedness nor cavity is seen over the whole surface, indicating that the cast alloy is composed of an amorphous phase. Figure 14 shows the changes in σ_f, E and ε with V_f for the cast bulk amorphous $Zr_{60}Al_{10}(Cu–Fe)_{20}Pd_{10}$ cylinders with di-

ameters of 2.2 and 2.7 mm, respectively. The σ_f and E of the Pd-containing cast cylinder are 1760 MPa and 81.5 GPa, respectively, at $V_f=0\%$ and increase to 1880 MPa and 89.5 GPa, respectively, at $V_f=40\%$. The similar increase in mechanical properties by precipitation of the nanoscale $Zr_2(Cu, Pd)$ phase is recognized for the Fe-containing bulk alloy and the σ_f and E increase from 1750 MPa and 81.1 GPa, respectively, at $V_f=0\%$ to 1850 MPa and 85.6 GPa, respectively, at $V_f=28\%$. Furthermore, as exemplified in Fig. 15, we have confirmed that the tensile fracture mode consisting of a shear sliding, followed by an adiabatic failure remains to be unchanged in the V_f range up to 40% where the highest σ_f value is obtained and the further increase in V_f induces the change in the fracture mode to a brittle type characterized by the generation of a fracture surface perpendicular to the direction of tensile load.
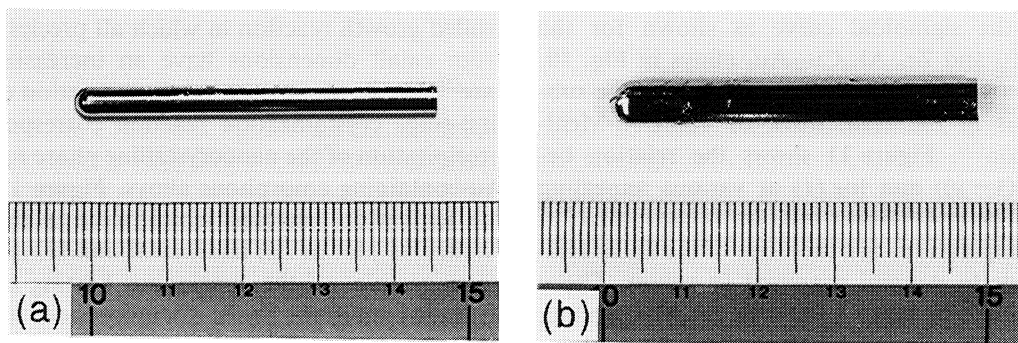

Fig. 13   Outer morphology of the cast bulk amorphous $Zr_{60}Al_{10}Cu_{20}Pd_{10}$ and $Zr_{60}Al_{10}Cu_{15}Pd_{10}Fe_5$ alloys with diameters of 4 and 6 mm, respectively.
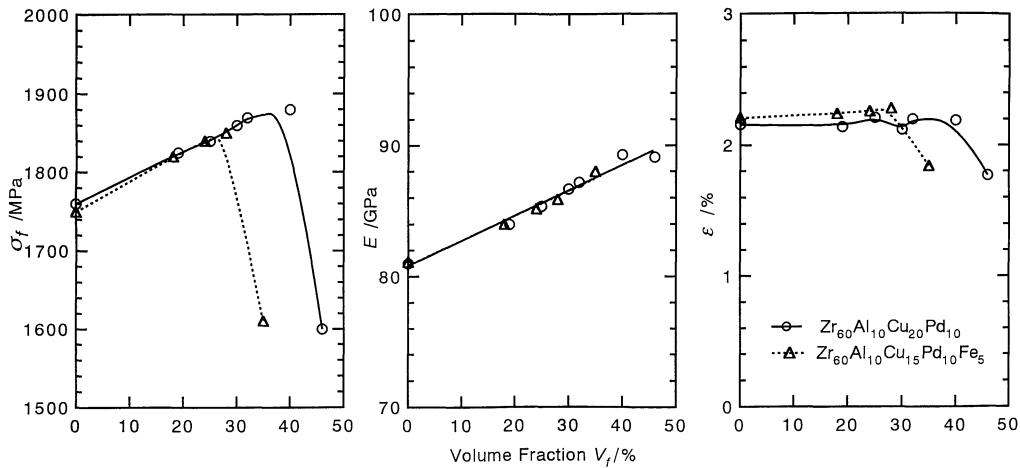
Fig. 14   Changes in the σ_f, E and ε with V_f of the Zr_2Cu for cast bulk amorphous $Zr_{60}Al_{10}Cu_{20}Pd_{10}$ and $Zr_{60}Al_{10}Cu_{22}Au_8$ alloys.
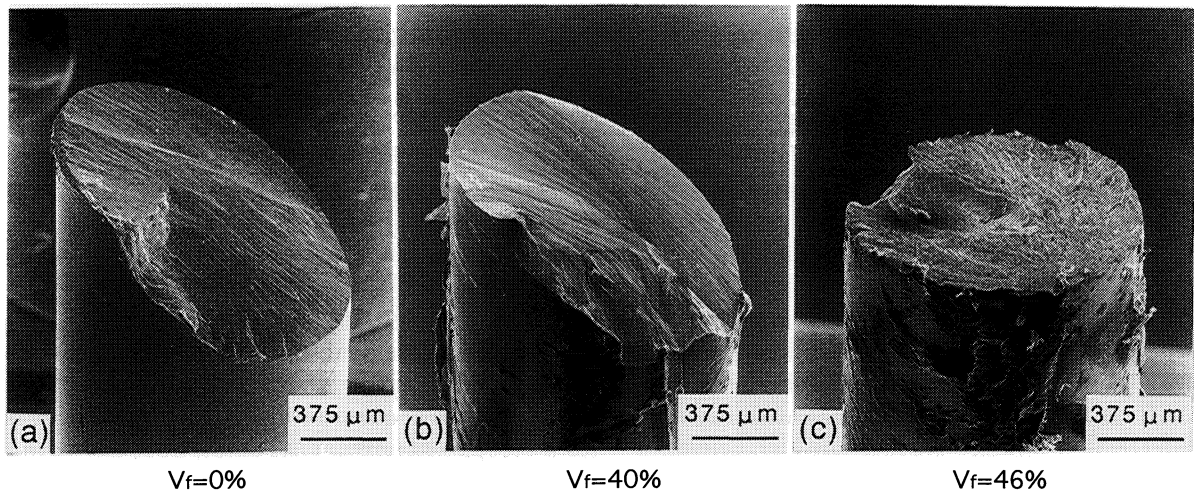

Fig. 15   Tensile fracture surface appearance of the cast bulk amorphous $Zr_{60}Al_{10}Cu_{20}Pd_{10}$ alloy. (a) $V_f=0\%$, (b) $V_f=40\%$, and (c) $V_f=46\%$.

IV.   Discussion

1.   Formation of the nanocrystalline structure

It was demonstrated that the crystallized structure of the $Zr_{65}Al_{7.5}Cu_{27.5}$ alloy caused by the polymorphic reaction consists of Zr_2Cu phase with large grain sizes of 400 to 500 nm, while the addition of Pd or Au element decreases drastically the grain size of $Zr_2(Cu, Pd)$ phase to less than 10 nm. The high-resolution TEM and nanobeam EDX analyses reveal that the Pd and Au elements are dissolved into the Zr_2Cu phase and the Al element is rejected from the compound phase and segregated into the remaining amorphous phase. The Avrami exponent values indicate that the nanocrystallization of the Pd- and Au-containing alloys proceeds by the diffusion-controlled growth reaction in which all precipitates growing from small dimensions have an increasing nucleation rate. We have also shown that the activation energy for the first-stage crystallization reaction corresponding

to the precipitation of the nanocrystalline phase is 3.2 to 3.6 eV for the $Zr_{60}Al_{10}Cu_{20}Pd_{10}$ alloy and 3.2 to 3.8 eV for the $Zr_{60}Al_{10}Cu_{22}Au_8$ alloy, which are much larger than that (1.9 to 2.2 eV) for the Zr-Al-Cu ternary alloy. Based on the above-described experimental results on the structural and kinetic analyses of crystallization, the formation process of the nanocrystalline $Zr_2(Cu, Pd)$ phase surrounded by a residual amorphous phase upon partial crystallization of the Zr-Al-Cu-Pd amorphous alloys is schematically shown in **Fig. 16**. It is generally known that the formation of a nanostructure from an amorphous phase requires the following three factors, *i.e.*, (1) a multistage crystallization mode leading to the precipitation of a primary crystalline phase, (2) the ease of homogeneous nucleation of the primary phase, (3) the difficulty of subsequent crystal growth reaction, and (4) a high thermal stability of the remaining amorphous phase. The addition of Pd or Au element with much larger negative heats of mixing against Zr causes the change of the crystallization mode from the single stage to the
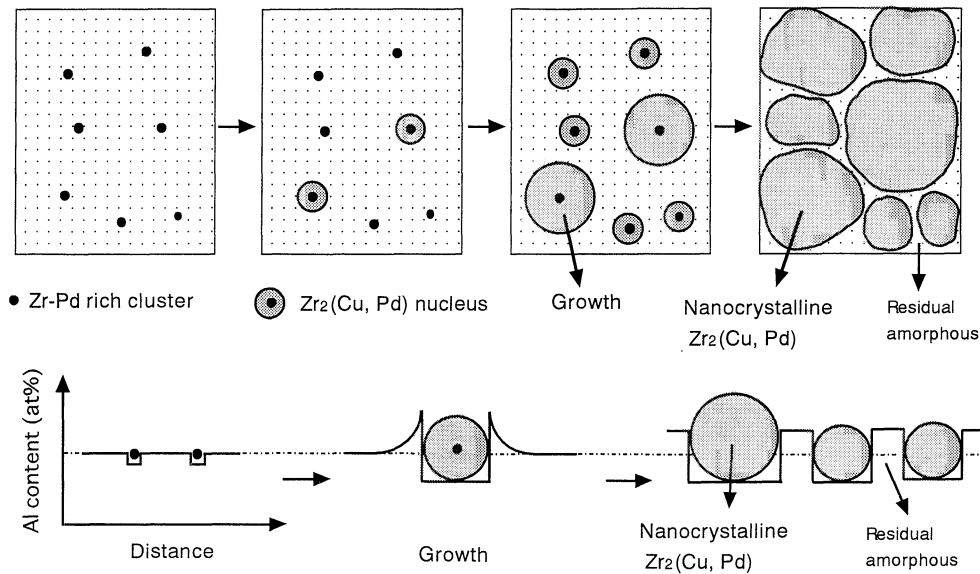
Fig. 16   Schematic illustration showing the formation process of nanocrystalline Zr₂(Cu, Pd) phase surrounded by residual amorphous phase and showing the change in the Al concentration in the Zr₂(Cu, Pd) and remaining amorphous phases during isothermal annealing.

two stages as well as the homogeneous generation of Zr–Pd or Zr–Au rich clusters, which can act as a nucleation site of the Zr₂(Cu, M) (M=Pd or Au) phase. The subsequent growth of the Zr–Pd rich cluster is also difficult because of the enrichment of the Al element in the remaining amorphous phase near the interface between amorphous and Zr₂(Cu, Pd) phases resulting from the elimination of Al from the Zr₂(Cu, Pd) phase. The difficulty of the growth reaction seems to result in the high activation energy for the precipitation of the Zr₂(Cu, Pd) phase. Furthermore, the enrichment of the Al element also induces the increase of the thermal stability of the remaining amorphous phase against crystallization. The increase of the thermal stability also plays an important role in the maintenance of the nanoscale size of the primary crystalline phase.

2. High tensile strength combined with good ductility for the nanostructure alloys

In the present results, it should be noticed that the nanostructure alloys consisting of nanoscale Zr₂(Cu, Pd) or Zr₂(Cu, Au) compound particles surrounded by the remaining amorphous phase exhibit good bending ductility and high tensile fracture strength in the V_f range up to about 70% for the melt-spun ribbons and about 20 to 40% for the cast bulk cylinders. Here, we consider the reason why the nanoscale compound-base alloys can have good ductility and high tensile strength. In particular, the nanostructure alloys in a melt-spun ribbon form are also regarded as a new type of mixture consisting of nanoscale compound grains (with a size of 5 to 15 nm) and amorphous intergranular phase (with a V_f of about 30%). The deformation of the nanostructure alloys by bending or tensile stress is thought to occur by sliding of the amorphous intergranular phase. The present result is believed

to be the first synthesis of high-strength and high-ductility alloys via amorphous intergranular sliding among intermetallic compounds at room temperature. The maintenance of good bending ductility even at the high V_f of 75% is in contrast to the previous data[9][10] that the formation of the ductile nanostructure alloys is limited to the small V_f range below about 30%. We have also confirmed that the above-described anomalous ductile behavior is recognized only for the amorphous alloy exhibiting the glass transition phenomenon. Consequently, the reason why the nanostructure alloys consisting of Zr₂Cu phase surrounded by the amorphous intergranular phase exhibit good bending ductility and high tensile strength is presumably due to the combination of the following four factors, i.e., (1) the residual amorphous phase can contain a large amount of free volumes by annealing in the supercooled liquid region, followed by water quenching, (2) the amorphous/Zr₂Cu interface has a high degree of packing fraction because of a much lower interface energy at the liquid/solid interface[26], (3) the Zr₂Cu with a uniform particle size disperses homogeneously, (4) the Zr₂Cu disperses isolately in coexistent with an amorphous intergranular phase, and (5) the remaining amorphous phase has high thermal stability resulting from the enrichment of solute elements. The optimum V_f leading to the maximum values of σ_f is about 20 to 40% for the cast bulk alloys and considerably lower than that (about 70%) for the melt-spun ribbons. The distinct difference seems to originate from the lower cooling rates during water quenching from the annealing temperature between T_g and T_{x1} for the bulk samples. That is, the amount of free volumes introduced by water quenching is considerably lower for the bulk samples than for the ribbon samples, leading to the lower values of the optimum V_f for the bulk samples.

V. Conclusions

The first success of synthesizing bulk amorphous alloys containing a nanoscale crystalline phase and the achievement of high tensile strength exceeding that for the amorphous single phase alloys are encouraging for future development of bulk amorphous alloys with further useful characteristics and with large dimensions. The progress of the fundamental study along the present research direction is expected to enable the syntheses of Fe- and Co-based bulk nanocrystalline alloys with various functional characteristics of soft magnetism, hard magnetism, highly sensitive magnetostriction, superplasticity etc. In combination with the future progress of bulk amorphous alloys, bulk nanocrystalline alloys containing the remaining amorphous phase are expected to be rapidly developed as a new type of metallic functional materials in the near future.

REFERENCES

(1) J. J. Croat, J. F. Herbst, R. W. Lee and F. E. Pinkerton: J. Appl. Phys., 55 (1984), 2078.
(2) R. Coehoorn, D. B. De Mooij and C. De Waard: J. Magn. Magn. Mater., 80 (1989), 101.
(3) A. Inoue, A. Takeuchi, A. Makino and T. Masumoto: Mater. Trans., JIM, 36 (1995), 676.
(4) Y. Yoshizawa, S. Oguma and K. Yamaguchi: J. Appl. Phys., 64 (1988), 6044.
(5) K. Suzuki, N. Kataoka, A. Inoue, A. Makino and T. Masumoto: Mater. Trans., JIM, 31 (1990), 743.
(6) Y. H. Kim, A. Inoue and T. Masumoto: Mater. Trans., JIM, 31 (1990), 747.
(7) H. Chen, Y. He, G. J. Shiflet and S. J. Poon: Scripta Met., 25 (1991), 1421.
(8) S. G. Kim, A. Inoue and T. Masumoto: Mater. Trans., JIM, 32 (1991), 875.
(9) A. Inoue: Materia Japan, 36 (1997), 926.
(10) A. Inoue, Y. Tanaka, Y. Miyauchi and T. Masumoto: Sci. Rep. Res. Inst. Tohoku Univ., A39 (1994), 147.
(11) A. Inoue, K. Ohtera, K. Kita and T. Masumoto: Jpn. J. Appl. Phys., 27 (1988), L2248.
(12) A. Inoue, T. Zhang and T. Masumoto: Mater. Trans., JIM, 30 (1989), 965.
(13) A. Inoue, T. Zhang and T. Masumoto: Mater. Trans., JIM, 31 (1990), 177.
(14) A. Inoue, T. Shibata and T. Zhang: Mater. Trans., JIM, 36 (1995), 1420.
(15) A. Peker and J. S. Gook: Appl. Phys. Lett., 63 (1993), 2342.
(16) A. Inoue and J. S. Gook: Mater. Trans., JIM, 36 (1995), 1180.
(17) A. Inoue, N. Nishiyama and T. Matsuda: Mater. Trans., JIM, 37 (1996), 1332.
(18) Y. He and R. C. Schwarz: Met. Trans., in press.
(19) A. Inoue, T. Zhang and T. Itoi: Mater. Trans., JIM, 38 (1997), 359.
(20) A. Inoue, T. Zhang and A. Takeuchi: Appl. Phys. Lett., 71 (1997), 464.
(21) A. Inoue, M. Koshiba, T. Itoi and A. Makino: Appl. Phys. Lett., 73 (1998), No. 6, in press.
(22) C. Fan and A. Inoue: Mater. Trans., JIM, 38 (1997), 1040.
(23) W. A. Johnson and R. F. Mehl: Trans. AIME, 135 (1939), 416.
(24) F. S. Ham: J. Appl. Phys., 30 (1959), 915.
(25) J. W. Christian: The Theory of Transformations in Metals and Alloys, Pergamon Press, Oxford, (1975), p. 542.
(26) E. S. Machlin: Thermodynamics and Kinetics, Giro Press, New York, (1991), p. 125.